Journal of Applied Mechanics. Received December 21, 2020;
Accepted manuscript posted January 25, 2021. doi:10.1115/1.4049954

Structural Mechanics of Negative Stiffness Honeycomb Metamaterials

Navid Mehreganian[1], Arash S. Fallah[2], and Pooya Sareh[1*]

[1] Creative Design Engineering Lab (Cdel), Department of Mechanical, Materials, and Aerospace Engineering, School of Engineering, University of Liverpool, Liverpool, L69 3GH, United Kingdom

[2] Department of Mechanical, Electronic, and Chemical Engineering, OsloMet, Pilestredet 35, St. Olavs plass, Oslo NO-0130, Norway

** Corresponding author. Email: pooya.sareh@liverpool.ac.uk*

Abstract. The development of multi-stable structural forms has attracted considerable attention in the design of architected multi-materials, metamaterials, and morphing structures, as a result of some unusual properties such as negative stiffness and, possibly, negative Poisson's ratio. Multi-stability is achieved through a morphological change of shape upon loading, and in doing so multi-stable structures undergo transitions from one equilibrium state to another.

This paper investigates the structural performance of the negative stiffness honeycomb (NSH) metamaterials made of double curved beams which are emerging in various applications such as sensors, actuators, and lightweight impact protective structures with structural tunability and recoverability. An analytical treatment is pursued using the Euler-Lagrange theorem and the stability of the honeycomb has been studied. Based on a static analysis of the nonlinear elastic system, the developed tangent stiffness matrix and ensuing deformation curve were assessed through multiple phases of deformation. The closed-form solution was in good agreement with the numerical finite element model at different bistability ratios. It was shown that the bistability ratio had a pronounced effect on the overall response of the honeycomb and the desired negativity in the stiffness matrix could be achieved with high bistability ratios.

Keywords

Mechanical metamaterial; Negative stiffness; Honeycomb structure; Snap-through buckling; Curved beam

Journal of Applied Mechanics. Received December 21, 2020;
Accepted manuscript posted January 25, 2021. doi:10.1115/1.4049954

Nomenclature

Latin upper-case		*Latin lower-case*		*Greek upper- and lower-case*	
A_j	Displacement field amplitude of the j^{th} mode, [1]	b	Beam width, $[L]$	Ω	Excitation frequency, $[T^{-1}]$
A	Closed surface Area, $[L^2]$	d	Deformation of mid-span, $[L]$	$\boldsymbol{\Delta}$	Vector form of the mid-point displacement of the curved beam, $[L]$
C	Amplitude of displacement; [L]	f	Axial compression load, $[MLT^{-1}]$	Δ	Dimensionless mid-point displacement of the curved beam, $[L]$
E	Young's Modulus, $[ML^{-1}T^{-2}]$	h	Midpoint displacement of straight beam, $[L]$	$\overline{\Delta}$	Total dimensionless displacement of the structure, $[L]$
$F(x)$	Harmonic excitation load, $[MLT^{-2}]$	$\bar{h}$	Bistability ratio, [1]	ω_0	Eigenvalues, [1]
I	Second moment of area, $[L^4]$	k_i	Stiffness of the i^{th} member, $[MT^{-2}]$	ω_j	Modal frequency, [1]
$\boldsymbol{K}$	Tangent stiffness matrix, $[MT^{-2}]$	l_0	Beam span, $[L]$	τ	Section thickness, $[L]$
L_x	Characteristic length of the structure, $[L]$	m_b	Inertia mass of the curved beam, $[M]$	$\bar{\zeta}$	Damping coefficient, $[MT^{-1}]$
P	Equivalent concentrated lateral load, $[MLT^{-2}]$	q_0	Load per unit length, $[MT^{-2}]$		
$\bar{P}$	Dimensionless concentrated lateral load, $[MLT^{-2}]$	p	Membrane force, $[MLT^{-2}]$		
U_b	Bending strain energy, $[ML^2T^{-2}]$	s	Length of the curved beam after deformation, $[L]$		
U_m	Membrane strain energy, $[ML^2T^{-2}]$	s_0	Initial length of the curved beam, $[L]$		
U_s	Elastic potential energy, $[ML^2T^{-2}]$	r	Radius of gyration, $[L]$		
W_0	Original configuration of the curved beam, $[L]$	$\hat{t}$	Scaled time, $[T]$		
W_1	Transverse displacement of the straight beam, $[L]$	$\overline{w}_j$	Dimensionless displacement field of the j^{th} mode; [1]		
		$\boldsymbol{w}$	Vector array form of the beam mid-span displacement, $[L]$		
		$\overline{\boldsymbol{w}}_{\boldsymbol{0}}$	Dimensionless vector form of the beam mid-span displacement, $[L]$		

1 Introduction

The development of multi-stable structural forms and manufacturing techniques, alongside a better understanding of fundamental nonlinear theories of continuum mechanics, have allowed the fabrication of lightweight structures composed of slender structural elements with high load-bearing capacity. These adaptive forms undergo shape change while providing appreciably high strength, thus offering a basis for the design of morphing structures. Various methods exist to render multi-stability in structural elements feasible, such as applying pre-stress [1], thermal effects [2], and curvature [3].

With recent advancements in additive manufacturing technologies, there has been a lot of interest in the structural mechanics of honeycomb structures, owing, not only to their relatively high stiffness and strength, but also to their efficient specific energy absorption during accidental impacts [4], [5]. These structures feature a large constant plateau in their stress-deformation path between the initial yield and the densification point. Although the relative density is a prime factor [5]–[7] in the mechanical performance of lattice/honeycomb structures, other factors such as cell wall angle, loading conditions, cell structure, and geometry also play important roles. For instance, hexagonal honeycomb structures subjected to compressive loading exhibit different buckling modes depending on the loading condition. In uniaxial compression, two kinds of cell collapse appear and alternate in the loading direction as a result of cell wall buckling, while in biaxial compression the buckled cell pattern entails two orthogonal axes of symmetry [8].

In previous studies in this area, Zheng et al [9] presented a finite element model for the dynamic crushing of the hexagonal honeycomb structures. Hu et al. [10], [11] investigated the same problem, experimentally as well as computationally, but with the influence of the cell wall angle and impact velocity on the crushing behaviour included. By assuming the beam element behaviour for the members, they showed that in honeycombs experiencing high-velocity impacts, a localised crushing band occurs at the loading band normal to the impact direction, which propagates layer by layer to the supporting ends, while the honeycombs with increased cell wall angles, at impact velocities above 40m/s, undergo deformation modes similar to that of high-velocity impacts, regardless of the initial impact velocity.

A range of analytical [8], [12], experimental [13], [14], and numerical [13], [15] investigations were carried out on the mechanical behaviour of hexagonal honeycomb structures in the past. Ouyang et al. [16] studied the stress concentration in defective octagonal honeycombs (with missing cell walls along a row) subject to uniaxial tension. They found that the stresses in cell walls decrease exponentially with distance from the centre of the defect.

Previous studies [17], [18] analysed the static post-buckling response and dynamic vibration of buckled clamped-clamped beams subject to harmonic excitations theoretically and experimentally. Using the multi-mode Galerkin discretisation, the period-doubling bifurcation, snap-through and quasi-periodic motions were determined. The effective nonlinearity, or the quotient of the functional of the displacement field over a closed surface to the vibrational frequency, remained negative below the critical buckling level (buckled displacement at mid-span). The latter work determined exact solutions to the post-buckling of the beams with different boundary conditions. Li et al. [19] investigated the vibration of a thermally buckled beam with geometric nonlinearity effects considered in post-buckling analyses.

Journal of Applied Mechanics. Received December 21, 2020;
Accepted manuscript posted January 25, 2021. doi:10.1115/1.4049954

From the load-displacement curve viewpoint, the snap-through instability phenomenon is associated with a sudden jump in the displacement in the load-control curve. A counterpart phenomenon called snap-back, however, occurs in the displacement-control curve when the load reduces suddenly even without an increase in the prescribed displacement [20], [21]. Mechanical systems that do not dissipate energy undergo a loading-unloading cycle, thus achieving hysteresis usually in a displacement controlled way. References [20], [22] examined the instability of an RVE (representative volume element) mechanical system comprising two or more cosine-shaped, curved beams paired vertically in series, wherein the top beam is thinner than the bottom one. The hysteresis of the structure was examined under displacement-control loading and the difference with the load-control case was elucidated. Upon stretching at the edges, the curvature of the top slim beam changed while the bottom beam curvature remained relatively constant. For a lattice made of such an RVE, curvature reversing was observed in the middle beams which were shorter than the top and bottom ones. The slim beams exhibited snap-back buckling while the curvature of the bottom beam remained unchanged for various loading scenarios. In a similar study [23], the snap-back phenomenon of the thick hyperelastic columns was observed where both the force and displacement reduced after the onset of loading.

Mechanical systems that exhibit bistability are ideal candidates for some applications in areas such as robotics [24]–[26] and product design [27]–[29]. Experimental evidence demonstrated that the desired bistability in the double curved beams provides two distinct stable configurations. The transition of the buckled beam from one stable position to another is accompanied by the reduction of the force which results in the release of the absorbed energy [30], [31].

Bistable beam structures could be integrated into mechanical systems that absorb energy elastically to provide impact resistance, enabling them to recover from an initial impact and respond to subsequent impacts. Examples of such systems are negative stiffness honeycomb (NSH) metamaterials, which when subjected to lateral unidirectional loads, exhibit zero Poisson's ratio and Negative Stiffness as salient features. The terminology NSH refers to a decrease in load following an increase in displacement in the honeycomb structure. While the response of the NSH unit cell investigated by [32] was similar to the hexagonal honeycomb structure, the NSH structure (composed of an array of NSH cells) featured considerably higher recoverability (i.e., negligible plastic deformation) than the conventional hexagonal honeycomb structure. In the circumstances of frequent collisions, a structure made of these cells can be a viable choice. Pre-strain below the point of instability in NSH structures enables the tunability of bulk elastic wave propagation [33]. The authors examined Bloch wave solutions in the NSH at pre-strain values of 0, 0.0101, 0.0207, and 0.0252, and showed that the size and magnitude of the band gaps frequency range decreased with the increase in pre-strain.

Another structural system of interest pertains to acoustic metamaterials, because their sub-wavelength structure permits controllable wave dispersion. Vangbo [34] and Qiu and Lang [35], [36] proposed an analytical model for mechanically-bistable curved beams with a prefabricated geometric profile similar to that of a conventional beam deformed into the first Euler's buckling mode when subjected to an external concentrated force (actuation) at its mid-span. Analytical investigations were validated by microscale experimental models using an actuator. Cazottes et al. [30] studied the same problem for a single curved beam with the force applied at different locations. Camescasse [31] investigated the static actuation of an arch with initial constant curvature.

Despite the interesting studies mentioned above, research on NSH metamaterials is still in its infancy, given most studies have focused on negative stiffness honeycombs as lattice structures in rectangular patterns. This work proposes an analytical model to describe the structural mechanics of NSH metamaterials with potential application to the design of recoverable protective systems.

This paper is organised into five sections. Following this introduction, a mathematical model for the quasi-static loading of the bistable curved beam is developed. In Section 3, an analytical solution is sought for a transversely-loaded honeycomb structure, which is designed from the modular pattern of the clamped double curved beams, while local and global deformations are investigated accordingly. Section 4 examines the validity of the analytical model using numerical finite element models. Finally, Section 55 presents the conclusions of the study.

2 Governing Equations

The honeycomb model assessed herein, depicted in Figure 1a, is similar to the design proposed and examined by Correa et al. [32], [33]. The structure is architected with four pairs of double curved beams along the direction of the load and an arbitrary number of cells normal to this direction. It is stipulated that the model is restrained at either side with axisymmetric boundary conditions, while a case with unrestrained boundaries is discussed later in the context of the problem. The beams are connected with a series of horizontal and vertical stiffeners of identical thickness.

The structure is subject to a static, uniformly-distributed compressive load q_0 [force/length], which is exerted laterally, replicating a unidirectional compression. However, as the upper row of double curved beams remains undeformed before the full axial squashing and snap-through of the double curved beams on the lower rows, the equivalent point load exerted at the mid-spans of the double curved beams may be considered in the study. It is further assumed that the structure remains purely elastic throughout the loading process.

The deformation of the NSH model, following the experimental and numerical evidence, occurs in four stages, namely (i) the downward motion resulting in the axial compression of the structure struts, (ii) the snap-through in the inverted beams of the top row, (iii) further axial compression, and finally (iv) the snap-through of the roof-shaped curved beams in the lower row. Throughout the motion, the kinematic admissibility of the displacement field and the stress state are ensured so that there are no ‘jumps’ in the deformation.

The curved beams, as fabricated, have a sinusoidal profile, which mimics a monolithic beam buckled into its first Euler buckling mode (see Figure 1b). Upon the application of loads, the double curved beams exhibit bistability [36], i.e., the system jumps abruptly from mode 1 to 3 without going through mode 2 (see Figure 1c). Thus, the deformation of the double curved beams may be assumed to be homogeneous with no relative displacements of the top beam to that of the bottom. Hence, the pairing of the beams ensures that mode 2 is constrained, and the influence of this mode can be ignored.

Journal of Applied Mechanics. Received December 21, 2020;
Accepted manuscript posted January 25, 2021. doi:10.1115/1.4049954

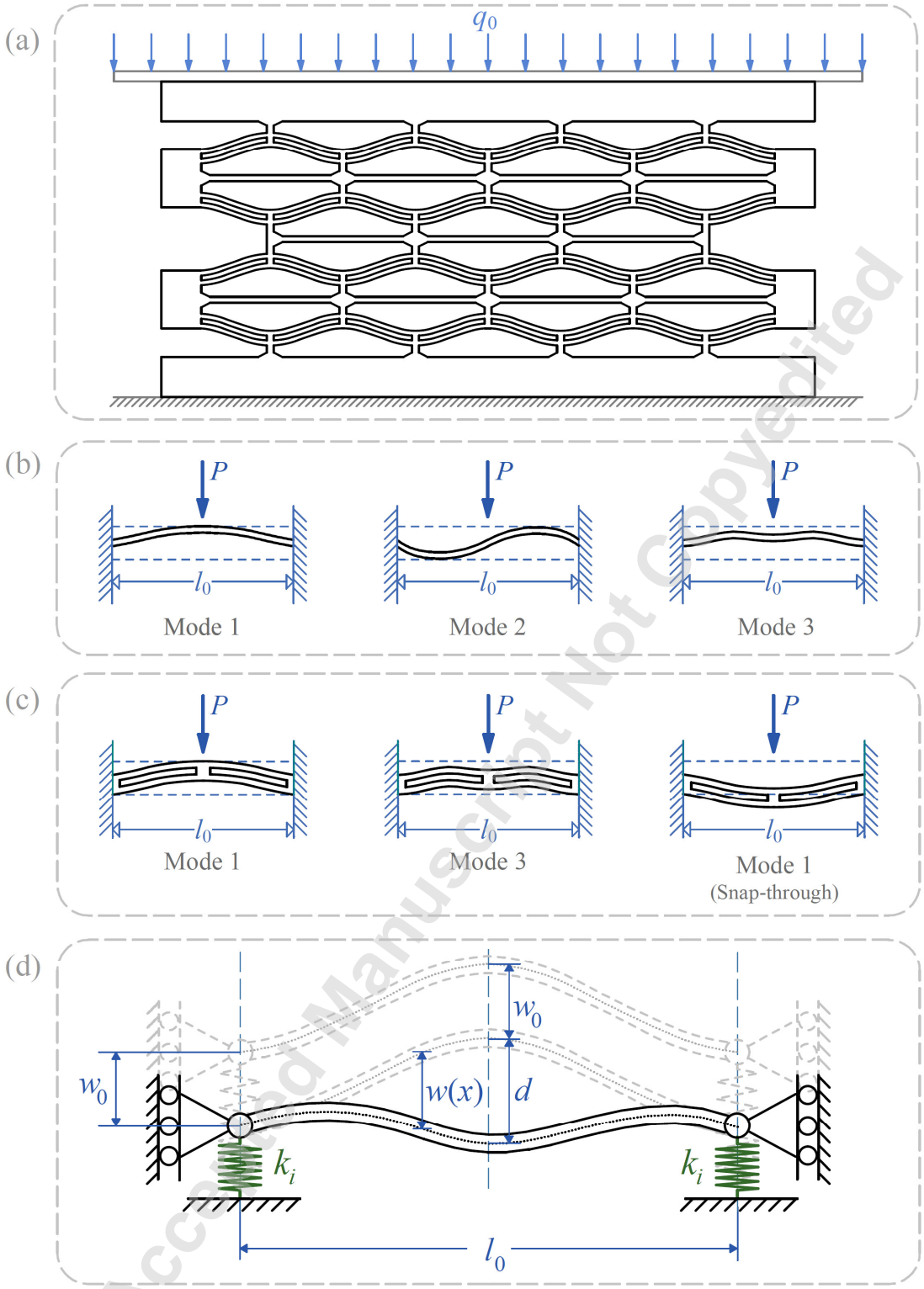

Figure 1. (a) NSH model for analytical study. (b) Buckling modes of the single curved beam with axisymmetric boundary conditions. (c) Buckling modes of the double curved beams with axisymmetric boundary conditions. (d) Deformation of the curved beam subject to a concentrated transverse load.

Journal of Applied Mechanics. Received December 21, 2020;
Accepted manuscript posted January 25, 2021. doi:10.1115/1.4049954

2.1 Buckling of the curved beam

Consider an initially flat beam with a rectangular cross-section of thickness τ, width b, and length l_0, which is made of an isotropic, ductile material, with clamped edges and subjected to a static axial load of magnitude f. The deformation response of the beam, when subjected to damped dynamic excitation is evaluated from the partial differential equation

$$m_b\frac{\partial^2 W_1}{\partial t^2}+f\frac{\partial^2 W_1}{\partial x^2}+EI\frac{\partial^4 W_1}{\partial x^4}+\zeta\frac{\partial W_1}{\partial t}-\frac{EA}{2l_0}\frac{\partial^2 W_1}{\partial x^2}\int_0^{l_0}\left(\frac{\partial W_1}{\partial x}\right)^2 dx=F(x)cos\Omega t, \tag{1}$$

where $\hat{\zeta}$ represents the damping coefficient, and $F(x)$ and Ω denote the excitation load and frequency, respectively. The prescribed initial and Dirichlet boundary conditions for a clamped-clamped beam are $W_1(x,t=0)=\left(\frac{\partial W_1}{\partial t}\right)_{t=0}=0$ and $W_1(0,t)=W_1(l_0,t)=\left(\frac{\partial W_1}{\partial x}\right)_{x=0}=\left(\frac{\partial W_1}{\partial x}\right)_{x=l_0}=0$, respectively. For convenience and generalisation, the following dimensionless parameters are introduced

$$\bar{x}=\frac{x}{l_0},\quad \overline{W_1}=\frac{W_1}{h},\quad \hat{t}=\frac{t}{l_0^2}\sqrt{\frac{EI}{m_b}},\quad \hat{f}=f\frac{l_0^2}{EI},\quad \hat{\zeta}=\frac{\zeta l_0^2}{\sqrt{m_bEI}},\quad \hat{F}(x)=F\frac{l_0^2}{EI},$$

$$\bar{\Omega}=ml_0^2\sqrt{\frac{EI}{m_b}},\qquad \text{and}\qquad \Gamma=\frac{h^2}{2r^2}\int_0^1 \overline{W_1}'^2 d\bar{x}, \tag{2a-h}$$

where $r=\sqrt{I/A}$ is the radius of gyration, while noting that the integral on the left-hand side of Eq. (1) is constant. The partial differential equation of Eq. (1) boils down to a fourth-order differential equation as

$$\ddot{\overline{W}}_1+\left(\hat{f}-\Gamma\right)\overline{W}_1''+\overline{W}_1^{iv}+\hat{\zeta}\dot{\overline{W}}_1=\hat{F}cos\bar{\Omega}\hat{t}. \tag{3}$$

As a convention, the overdot accounts for differentiation with respect to scaled time $\hat{t}$, while the prime represents differentiation with respect to a scaled coordinate $\bar{x}$. Provided that the temporal terms are eliminated, the two types of the solution to Eq. (3) are subsequently determined as

$$\overline{W_1}(\bar{x})=C(1-\cos(\omega_0\bar{x})), \tag{4}$$

$$\text{and}\quad \overline{W_1}(\bar{x})=C(1-2\bar{x}\ -\cos(\omega_0\bar{x})+2\sin(\omega_0\bar{x})/\omega_0), \tag{5}$$

where the Dirichlet boundary conditions $\overline{W_1}(0)=\overline{W_1}(1)=(\overline{W_1}')_{\bar{x}=0}=(\overline{W_1}')_{\bar{x}=1}=0$ are applied, whilst $\omega_0=\sqrt{\hat{f}-\Gamma}$ represents the critical buckling load. These boundary conditions result in four simultaneous equations, which, when cast in the matrix form, and dictating its determinant to be zero, yield the real solution. Subsequently, a restriction on ω_0 is imposed as

$$\sin\left(\frac{\omega_0}{2}\right)\left(\tan\left(\frac{\omega_0}{2}\right)-\frac{\omega_0}{2}\right)=0, \tag{6}$$

giving eigenvalues $\omega_0 = 2\pi,\ 2.86\pi, \dots$, and critical buckling loads $P_c = 4\pi^2, 8.18\pi^2, \dots$. Substituting Eqs. (4) and (5) into Eq. (2g) and making use of Eq. (6) gives constant $C = \pm\sqrt{\hat{f}/\omega_0^2 - 1}$. Thus, C can be determined from a given axial load for any required Eigenmodes [18].

Eqs. (1) and (4) represent the first and second buckling modes; the latter never occurs due to higher energy demand [30]. Hence, the original configuration of the fabricated beam in the study has a profile similar to the first Euler's buckling mode ($\omega_0 = 2\pi$):

$$W_0 = \frac{h}{2}\left(1 - \cos\left(\frac{2\pi x}{l_0}\right)\right), \tag{7}$$

where h is the rise of the beam. The respective profiles of the beam in its original and deformed configurations are illustrated in Figure 1d.

The foregoing analysis establishes a basis for the mathematical treatment of bucking in the honeycomb systems made of such curved beams. Similar to [36], a mode superposition analysis is performed to investigate the deformation of the curved beam. To this end, the system may be regarded as a discrete elastic system of n degrees of freedom depending on the number of cells. The buckling modes of deformation form an orthogonal set, which, having the same boundary conditions, collectively characterise the deflection of the beam when mode superposition is implemented. The deflection of the beam truncates as a linear combination of the modes as

$$w_j = h\sum_{j=1}^{\infty} A_j\left(1 - cos\left(\frac{\omega_j x}{l_0}\right)\right), \tag{8}$$

where modal frequencies ω_j are expressed as

$$\omega_j = (j+1)\pi, \qquad j = 1,3,5, \dots. \tag{9}$$

The frequencies of even subscripts are determined by the solution to Eq. (6). The lateral displacement at the mid-span of the beam is denoted as $d = W_1\left(\frac{l_0}{2}\right) - w\left(\frac{l_0}{2}\right)$. The bending strain energy U_b, the membrane strain energy U_m, and the total elastic potential energy U_s of the system are expressed, respectively, as

$$U_b = \int_0^{l_0}\left(\frac{\partial^2 W_1}{\partial x^2} - \frac{\partial^2 w}{\partial x^2}\right)^2 dx, \tag{10}$$

$$U_m = -\int_0^{l_0} pds, \tag{11}$$

$$\text{and } U_s = \frac{1}{2}\boldsymbol{w}^T\boldsymbol{K}\boldsymbol{w}, \tag{12}$$

Journal of Applied Mechanics. Received December 21, 2020;
Accepted manuscript posted January 25, 2021. doi:10.1115/1.4049954

where $\boldsymbol{w}$ represents the vector array form of the mid-span deformation d. Notably, by assuming the vertical struts to be inextensible, the transverse displacement of the curved beam mid-span in the bottom layer is identical to the axial deformation of the vertical struts in the top layer.

To evaluate Eq. (11), using the approximation $ds = dx\sqrt{1+\left(\frac{dw}{dx}\right)^2} \cong 1+\frac{1}{2}\left(\frac{dw}{dx}\right)^2$, the new length of the curved beam after deformation can be written as

$$s = \int_0^{l_0} 1+\frac{1}{2}\left(\frac{dw}{dx}\right)^2 dx. \tag{13}$$

The initial length of the beam, s_0, is therefore recovered by replacing w with W_1 in Eq. (13). The membrane force induced by the change of beam length is expressed as

$$p = Eb\tau\left(1-\frac{s}{s_0}\right). \tag{14}$$

Eqs. (8), (10), (11), and (14) construct the basis of the mathematical procedure to verify the buckling response of the curved beam. The overall lateral deformation of the structure is evaluated using Eq. (12). For brevity in the mathematical procedure, it is presumed that the local curved beam buckling at the onset of snap-through (or snap-back) and the global lateral deformation of the structure are independent, i.e. they do not occur simultaneously. In practice, the variation of the force at different phases is the algebraic sum of that of the local buckling together with that due to the global lateral deformations.

The following dimensionless parameters are utilised in this work

$$\bar{w}_j = \frac{w_j}{h}, \quad \bar{l} = \frac{l_0}{h}, \quad \bar{h} = \frac{h}{\tau}, \quad \bar{U}_b = \frac{U_b l_0^3}{EIh^2}, \quad \bar{U}_m = \frac{U_m l_0^3}{EIh^2}, \quad \bar{P} = \frac{Pl_0^3}{EIh},$$
$$\bar{x} = \frac{x}{l_0}, \quad \Delta = \frac{d}{h}, \quad \bar{s} = \frac{sl_0}{h^2}, \quad \bar{\boldsymbol{K}} = \frac{l_0^3}{EI}\boldsymbol{K}, \quad \text{and} \quad \bar{p} = \frac{fl_0^2}{EI}. \tag{15a-k}$$

The displacement profile is thus furnished as

$$\bar{w}_j = \sum_{j=1}^{\infty} A_j\left(1-cos\left(\omega_j\bar{x}\right)\right). \tag{16}$$

Substituting Eqs. (15) and (16) into Eqs. (10)-(14), the dimensionless parameters of Eqs. (15a-k) are calculated as follows

$$\Delta = 1-2\sum_{j=1,5,9,..} A_j, \tag{17}$$

$$\bar{s} = \left(\bar{l}^2 + \sum_{j=1}^{\infty}\frac{\omega_j^2 A_j^2}{4}\right), \tag{18}$$

Journal of Applied Mechanics. Received December 21, 2020;
Accepted manuscript posted January 25, 2021. doi:10.1115/1.4049954

$$\bar{p} = \frac{3\bar{h}^2}{\bar{s_1}}\left(\frac{\omega_1^2}{4} - \sum_{j=1}^{\infty}\omega_j^2 A_j^2\right), \tag{19}$$

$$\text{and} \quad \bar{s}_1 = \frac{\omega_1^2}{16\bar{l}^2} + 1. \tag{20}$$

It is assumed that the fabricated curved beam is stress-free at $\Delta = 0$; therefore, the leading-order terms of Eqs. (10)-(12) are expressed as

$$\bar{U}_b = \frac{\omega_1^4}{4}\left(A_1 - \frac{1}{2}\right)^2 + \sum_{j=2}^{\infty}\frac{\omega_j^4 A_j^2}{4}, \tag{21}$$

$$\bar{U}_m = \frac{12l_0^2}{\tau^2}\left(\bar{s} - \frac{8\bar{s}^2}{\omega_1^2 + 16\bar{l}^2)}\right), \tag{22}$$

$$\text{and} \quad \bar{U}_s = \frac{1}{2}\overline{\boldsymbol{w_0}}^T\bar{\boldsymbol{K}}\overline{\boldsymbol{w_0}}, \tag{23}$$

where $\overline{\boldsymbol{w_0}}$ is determined by substituting $\boldsymbol{\Delta}$ in place of $\boldsymbol{w}$, where $\boldsymbol{\Delta}$ is the vector array form of Δ.

Utilising the Lagrange-Dirichlet theorem reduces the analysis to the test of positive definiteness of potential energy $\Pi(A_j)$ as a function of a set of modes where the equilibrium condition for the system is obtained using ${}^{\partial\Pi}/_{\partial A_j} = 0$. Applying the principle of conservation of energy, the variation of the total potential energy of the system at the new equilibrium state is expressed as

$$\begin{aligned}\partial(\bar{\Pi}) = \left(\frac{(\omega_1^4 - \bar{p}\omega_1^2)}{2}A_1 + 2\bar{P} - \frac{\omega_1^4}{4}\right)\partial A_1 \; + \sum_{j=2,3,4,6,7}^{\infty}\frac{\omega_j^4 - \bar{p}\omega_j^2}{4}\partial\left(A_j^2\right) \\ + \sum_{j=5,9,13,\ldots}^{\infty}\left(\frac{\omega_j^4 - \bar{p}\omega_j^2}{2}A_j + 2\bar{P}\right)\partial\left(A_j\right).\end{aligned} \tag{24}$$

It follows that the coefficients of $\partial(A_j)$ terms with $j = 1,5,9,..$ in Eq. (31) should be zero to satisfy the equilibrium condition. Thus

$$A_1 = \frac{\omega_1^4 - 8\bar{P}}{2\omega_1^4 - 2\bar{p}\omega_1^2}. \tag{25}$$

In a similar fashion, the higher modes with $j = 5,9,13,\ldots$ are delineated as

$$A_j = \frac{-4\bar{P}}{\omega_j^4 - \bar{p}\omega_j^2}. \tag{26}$$

The stability of the system is contingent upon the positive definiteness of Π. The equilibrium state is stable, according to the Lagrange-Dirichlet theorem [37], provided that

$$\frac{\partial^2(\bar{\Pi})}{\partial A_j^2} = \sum_{j=2,3,4,6,7,..}^{\infty} 2\frac{\omega_j^4 - \bar{p}\omega_j^2}{4} A_j + \sum_{j=1,5,9,13,...}^{\infty} \left(\frac{\omega_j^4 - \bar{p}\omega_j^2}{2} + 2\bar{P} - \frac{\omega_1^4}{4}\right) > 0. \tag{27}$$

In the case of a double curved beam, the second mode is mechanically-constrained without any effect of the other modes, which indicates that j can take a value as high as 3. Thus, from Eqs. (17), (19), (24), and (25), the first kind of solution is

$$\bar{P} = \frac{\pi^4\Delta\left(\left(12(\Delta-1)(\Delta-2)\bar{h}^2 + 16\right) + 4\pi^2/\bar{l}^2\right)}{8\bar{s}_1}, \tag{28}$$

which is similar to the results in [36]. The force-displacement curve with higher-order terms may get delineated iteratively. The second ($A_j = 0, j = 3,4,6,7,8, \ldots$) and third ($A_j = 0, j = 2,4,6,7,8, \ldots$) kinds of solution, achieved using Eqs. (19), (24), and (25), yield loads $\bar{P} = \pi^4(4.18 - 2.18\Delta)$ and $\bar{P} = \pi^4(8 - 6\Delta)$, respectively, that are independent of the bistability ratios. In the sequel, the global response of the structure is assessed by the breakdown of the deformation into its four phases.

3 Deformation of the NSH structural system

A finite element method is employed to compile the tangent stiffness matrix of the system from the principal minor matrices of the i^{th} member in Eq. (29)

$$\bar{\mathbf{k}}_{\boldsymbol{i}} = \begin{bmatrix} k_i & -k_i \\ -k_i & k_i \end{bmatrix}. \tag{29}$$

Evidently, except for the double curved beams, all the horizontal stiffeners and vertical struts are in series and the tangent stiffness matrix is symmetric. The symmetricity of the tangential stiffness matrix, however, may be violated when friction or damage emanate, leading to energy dissipation. Such a case could occur in circumstances when material exhibits plastic behaviour due to the contact between the horizontal stiffeners with the buckled beam pairs, or the overall compression of the system. The tangent stiffness matrix would consist of a symmetric part and an asymmetric part, whereby the stability is determined from the former. For non-symmetric matrices, the condition of stability limit (critical state) is only satisfied if $\boldsymbol{K}\delta\boldsymbol{q} = \mathbf{0}$, i.e. the case of neutral equilibrium, where $\boldsymbol{K}$ is the stiffness matrix and $\delta\boldsymbol{q}$ designates the variation of the generalised coordinate vector $\boldsymbol{q}$ [37]. Given that they remain undeformed throughout the motion, the horizontal stiffeners do not contribute to the overall stiffness of the structure, but they restrain the model against shearing deformations and tie the unit cells together. It is assumed that the loading conditions would not impose full compression which would otherwise result in the emergence of frictional forces. Hence, the total axial deformation of the system in the vertical direction is evaluated using Hook's law.

In axial compression, the dimensionless stiffness of each strut is simply expressed as $k_i = Al_0^3/IL_i$ with L_i being the length of the strut. Thus, the tangent stiffness of the curved beams, when neglecting the higher modes, is recovered from Eq. (29) and expressed as

Journal of Applied Mechanics. Received December 21, 2020;
Accepted manuscript posted January 25, 2021. doi:10.1115/1.4049954

$$k_1 = \frac{\left(\left(4 + 3(3\Delta^2 - 6\Delta + 2)\bar{h}^2\right)\bar{l}^2 + \pi^2\right)\pi^4}{2\bar{l}^2\bar{s}_1} \tag{30}$$

As illustrated in Figure 2a, the most substantial case of the negative stiffness phenomenon pertains to the bistability ratio in the range of 2.4 – 6. Further increase in $\bar{h}$ beyond 6, however, does not render such a phenomenon for the beam. The absolute magnitude of stiffness also decreases as the quotient of the beam length to its height increases (see Figure 2b). Along the vertical axes of symmetry, the system is composed of a series of interconnected spring elements with notations given in Figure 2c.

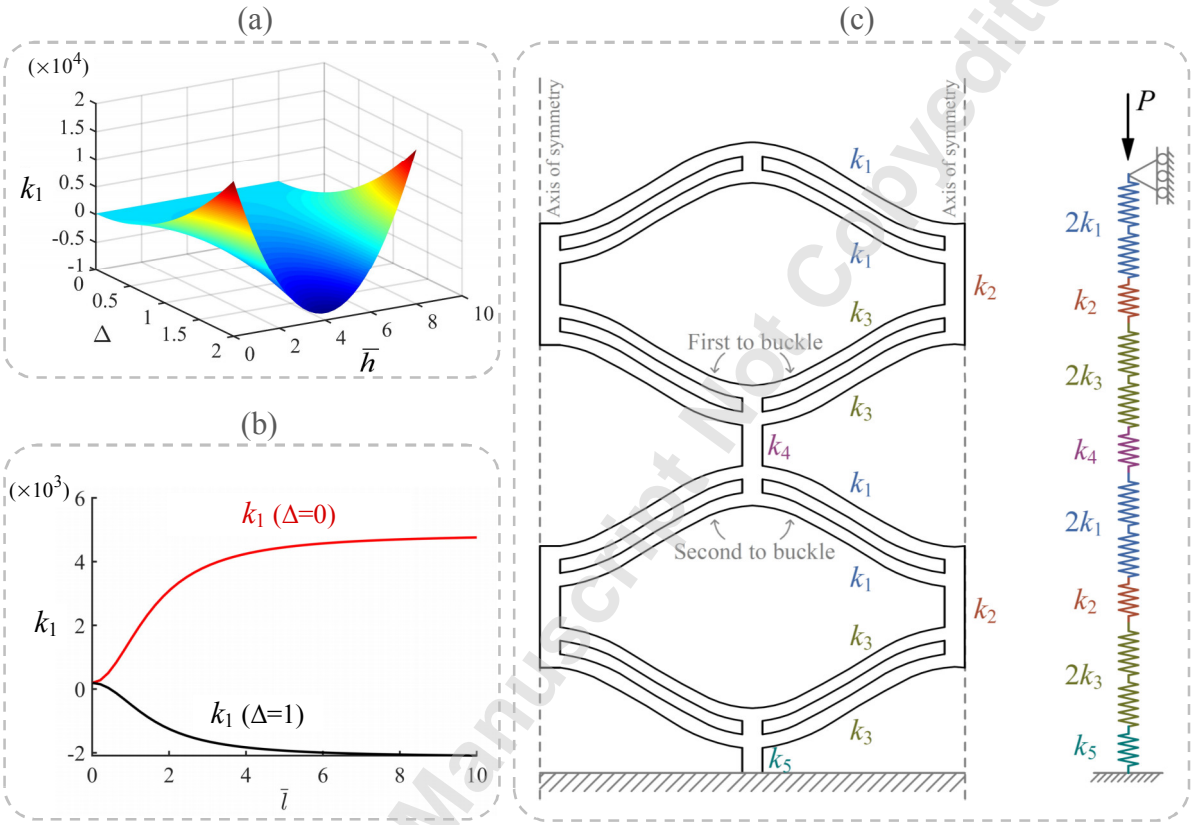

Figure 2 (a) Interaction of the bistability and deformation on the beam tangent stiffness. (b) Influence of the beam length on the curved beam tangent stiffness. (c) Designation of the stiffness of the curved beam in the model.

It is assumed that the stiffness of upright and inverted curved beams, respectively k_1 and k_3, are identical. The resultant stiffness matrix of the system, using the designation in Figure 2c, is expressed as

$$\boldsymbol{K} = 2\begin{bmatrix} k_1 & -k_1 & 0 & 0 & 0 & 0 & 0 & 0 \\ -k_1 & k_1+k_2 & -k_2 & 0 & 0 & 0 & 0 & 0 \\ 0 & -k_2 & k_2+k_3 & -k_3 & 0 & 0 & 0 & 0 \\ 0 & 0 & -k_3 & k_3+k_4 & -k_4 & 0 & 0 & 0 \\ 0 & 0 & 0 & -k_4 & k_4+k_1 & -k_1 & 0 & 0 \\ 0 & 0 & 0 & 0 & -k_1 & k_1+k_2 & -k_2 & 0 \\ 0 & 0 & 0 & 0 & 0 & -k_2 & k_2+k_3 & -k_3 \\ 0 & 0 & 0 & 0 & 0 & 0 & -k_3 & k_3+1/2k_5 \end{bmatrix} \tag{31}$$

Journal of Applied Mechanics. Received December 21, 2020;
Accepted manuscript posted January 25, 2021. doi:10.1115/1.4049954

Depending on the number of unit cells along the direction of loading, the deformation of the honeycomb structure is split into various phases each of which is associated with the consecutive buckling of the curved beams. The NSH metamaterial assessed herein is made of two modular cells (see Figure 2c and Figure 3) which may be visualised as two lumped masses M_1 and M_2 connected with springs, associated with which are the two displacement fields. The response of each unit cell is attributed to two main phases of deformation. The first phase corresponds to the small initial transverse deformation, while during the second phase the snap-through (snap-back) occurs. It transpires that the overall deformation is composed of four phases outlined as follows:

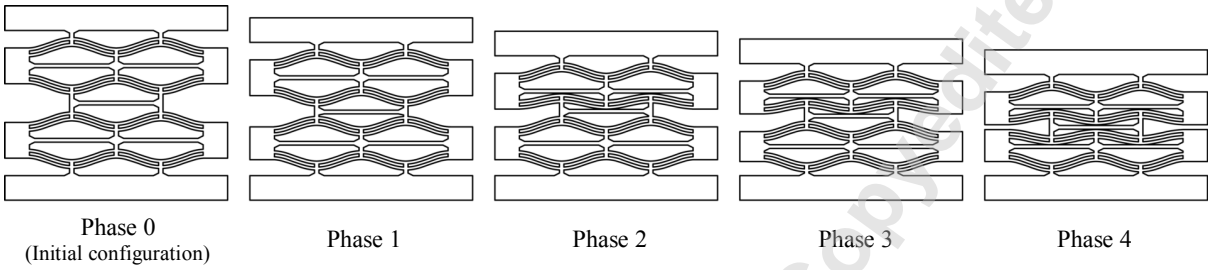

Figure 3 The presumed response of the NSH lattice at different phases of deformation according to [38]

Phase 1: Due to the evolution of normal stresses from the external load, both the inverted curved beams in the first (top) layer and the top curved beam in the lower layer experience simultaneous transverse displacements, following path OA (see Figure 4). It should be stressed that while the curved beam never reaches point A and remains at a point along the trajectory, the inverted beam continues to the point of zero stiffness. Points at A' and B' correspond respectively to the maximum and minimum loads determined by the static response of the curved beam [36] provided the higher modes are retained in the theoretical treatment, i.e. with $F = \pi^4(8 - 6\Delta)$. The magnitude of the force at A' diminishes below A as the bistability ratio increases beyond 2.7.

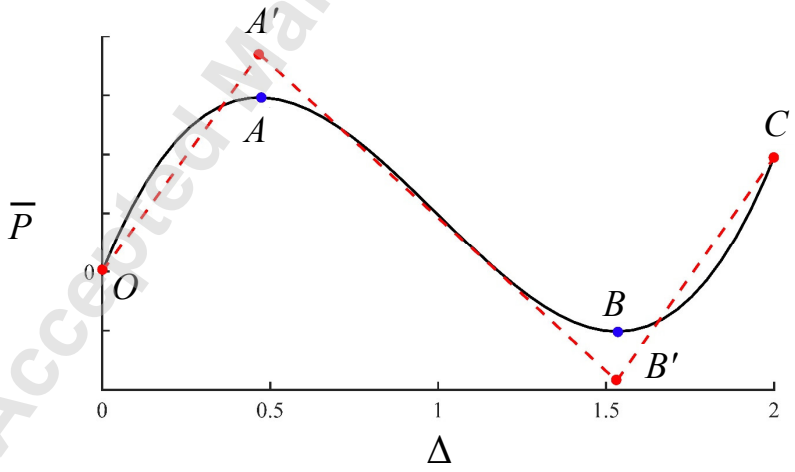

Figure 4 Simplification of the curved beam stiffness using the higher mode estimates ($j = 2$) for $\bar{P}$ and Δ from [36] at A' and B'

Phase 2: This phase triggers the onset of snap-through buckling in the inverted beam. The accumulated stress in the struts below the beam exerts a force of $\bar{P}/2$ upward. At this point, the second phase initiates with a jump (snap-through) in the beam, following path ABC from zero

curvature. The experimental results indicate that initially the k_3 elements reach a new equilibrium state following the snap buckling, before further downward motion commences, which highlights a curve *BC* in the force-displacement path.

Phase 3: Further loading is accompanied by a gradual rise in the deformation of the top curved beam in the lower level without snap-through buckling.

Phase 4: Note that Eq. (30) still holds for the calculation of the stiffness of the curved beam, with the value of Δ corresponding to the associated point *C* (see Figure 4) on the force-displacement curve of the inverted curved beam after the jump occurs (see Phase 3 in Figure 3) The structure continues to be compressed with the force-displacement curve reaching a plateau. Continuous loading leads to the snap-through of the top curved beam at the lower level. Thus, the $K_{55} - K_{66}$ components of the tangent stiffness matrix of the structure, corresponding to the buckled curved beam, are evaluated from Eq. (30) with $\Delta = 0$.

Following the work of [39] and numerical studies hereunder, it is assumed that the snap-through bucking in the lumped masses occurs consecutively as follows. At the transition point between each of the two phases, the displacement and resultant stresses are kinematically admissible.

4 Numerical analysis

4.1 Finite element model and results

A number of two-dimensional finite element (FE) models were set up in the software ABAQUS®14 for paramedic studies, for the purpose of investigating the bistability response of the structure by varying $\bar{h} = h/t$ and the validations of the analytical model. The FE models were discretised with a mesh of 27791 CPS4R plane stress elements, with 3 elements per curved beam thickness, reduced integration, and hourglass control, as depicted in Figure 5a. The out-of-plane width of the models was assumed to be 15mm to replicate the physical model. The NSH structure was bounded between two rigid surfaces, each discretised with 1200 R2D2 linear discrete rigid elements of characteristic length of 600mm. The model was made of Polyamide 11, which, with a Young's modulus of 1582MPa, a Poisson's ratio of 0.33, and a mass density of 1.04 g.cm^{-3}, is classified as a lightweight, isotropic, ductile, and highly flexible material. The models here were assumed to be perfectly elastic with prescribed geometric nonlinearities.

A Quasi-static loading condition was set up and the top surface was prescribed with a velocity of 0.01 mm/s for a period of 3000 seconds, while the bottom surface acted as a rigid boundary. A penalty contact with a coefficient of friction of 0.3 was assumed for each pair of the beams in contact. The geometry of the model is presented in Table 1 and Figure 5b.

The overall response of the NSH model to contact forces is similar to that of the unit cells experimented by [32], [38], whilst the local snap-through phenomenon occurred with the upper curved beams of the first level, compared to the experimental results which showed snap-through initially occurring in the top beams. Although there was relative displacement in some of the double curved beams, the overall deformed shape remained axially symmetric.

Journal of Applied Mechanics. Received December 21, 2020;
Accepted manuscript posted January 25, 2021. doi:10.1115/1.4049954

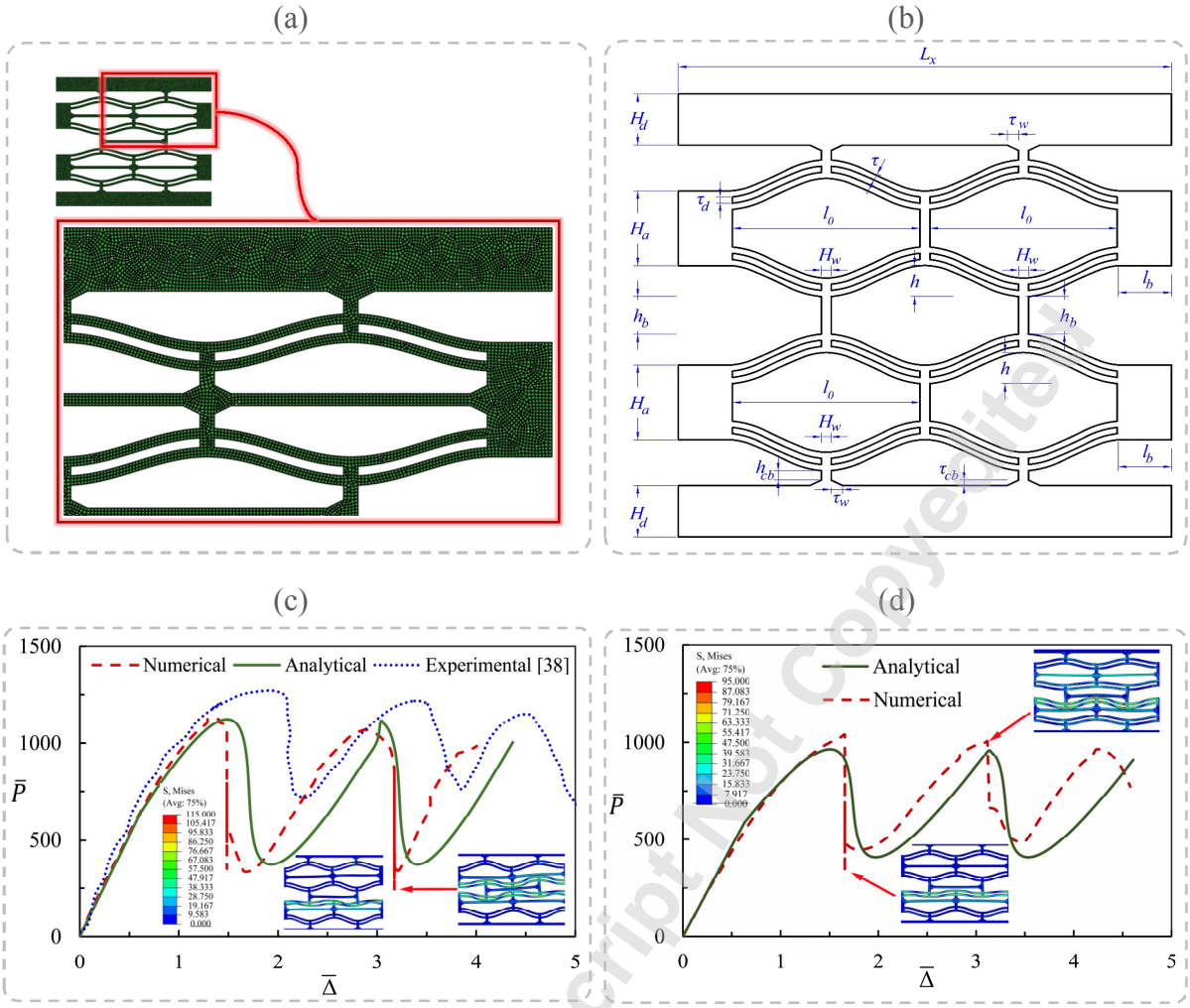

Figure 5 (a) Finite element mesh model for a typical NSH structure. (b) Geometric model of a typical NSH structure. (c) Comparison of our analytical and numerical models with the experimental results in [38] with $\bar{h} = 4$. (d) Comparison of our analytical and numerical models with $\bar{h} = 3.5$.

Table 1 Characteristic dimensions of the NSH model

Parameter	Magnitude (mm)	Parameter	Magnitude (mm)
H_d	16.5	l_0	57
H_a	24	l_b	16.5
H_w	3	τ	2
h	6,7,8,10,12	τ_{cb}	1.75
h_{cb}	3	τ_d	2
h_b	12	τ_w	3

The validation of the analytical model is conducted using the numerical outputs and the correlation of the results is plotted in Figure 5c-d when the influence of the higher modes ($j = 5,9, \ldots$) is ignored in the analyses. For comparison, the experimental results of [38] are normalised and plotted in Figure 5c. The difference between the experimental and analytical results is mainly due to the loading rate, accounting for the lag in the occurrence of the negative slopes. Furthermore, contrary to the numerical

models, no relative displacements between the beams was observed in the experiments. It should further be noted that, when having unrestrained edges at either side, there exists a horizontal component of the displacement field the magnitude of which was nearly 10% of the vertical one, in contrast to the experimental work by [38] with no discernible Poisson's ratio. The relative local horizontal deformations occurred between the springs and the vertical joints in all models (with restrained and unrestrained edges - as seen in Figure 6). While the analytical model fails to capture the local horizontal deformations occurring at the roof-shaped curved beams of the lower level, it estimates the force-displacement curve reasonably, with a slight shift in the occurrence of peaks. However, both the number of peaks in the FE model and the magnitude of the force at each peak corroborate with those of the analytical model. The highest shift in the deformation path is 12.6% which pertains to the models with $\bar{h} = 4$, while the general predicted trends of the state variables, i.e. deformation and force, in Table 2 are in good agreement.

Figure 6 compares the schematics of the deformation phases of the lattice and the force-displacement plots of the models with high bistability ratios. Clearly, the honeycomb models with values of $\bar{h}$ greater than 2 exhibit pronounced snap-through phenomenon, with considerable force reduction as the bistability ratio increases. However, the negative stiffness becomes less discernible with the bistability ratio of 5 and 6, as well as $\bar{h} < 3$, in accordance with the analytical prediction (Figure 2a).

As can be seen from Table 2, the maximum force captured from the numerical model at the onset of snap-through buckling compares favourably to the analytical counterparts, with less than 8% variations. A lower precision is observed when comparing the displacements at which the snap-through occurs. This is due to the discrepancies in the estimation of the deformation in the first phase of motion, characterised by a linear force-deformation path. It should also be noted that while the influence of the higher modes was neglected in the study, introducing a more sophisticated model by including higher modes would be at the expense of higher levels of mathematical complexity and simulation time, while having a minor impact on improving the accuracy of the results, which renders the analyses unnecessarily complicated. As such, provided the energy is dissipated by friction at the contact interface of the beams, the symmetry of the tangent stiffness matrix would be violated and thus the value of displacement is only an estimate in such a case.

A distinctive attribute observed in Figure 5 is the snap-back phenomenon occurring at $\bar{\Delta} \cong 1.5$ and $\bar{\Delta} \cong 3.3$, with the significant reduction in the force at constant displacement levels. While the analytical results predicted a smooth variation of the force in the vicinity of snap-back, the numerical counterpart encountered discontinuity, which can be elucidated as follows. First, at the former value of abscissa, there exists a symmetry breakdown in the buckling of the curved beams, e.g. while the beams at the bottom layer in the left unit cell of the lattice underwent a snap-back maintaining curvature symmetry, the curvature change in the adjacent beams on the right was not symmetric. Furthermore, the vertical and horizontal struts in this layer encountered some rotation, and the variation of the force at this point was not monotonic. Similarly, at $\bar{\Delta} \cong 3.3$, the shape of the double curve beams transitioned from a symmetric to a non-symmetric state, with some rotations in the horizontal beams, while such rotation was ignored in the analytical model for brevity. However, no such discontinuity was observed with $\bar{h} < 3.5$ (Figure 6b).

Journal of Applied Mechanics. Received December 21, 2020;
Accepted manuscript posted January 25, 2021. doi:10.1115/1.4049954

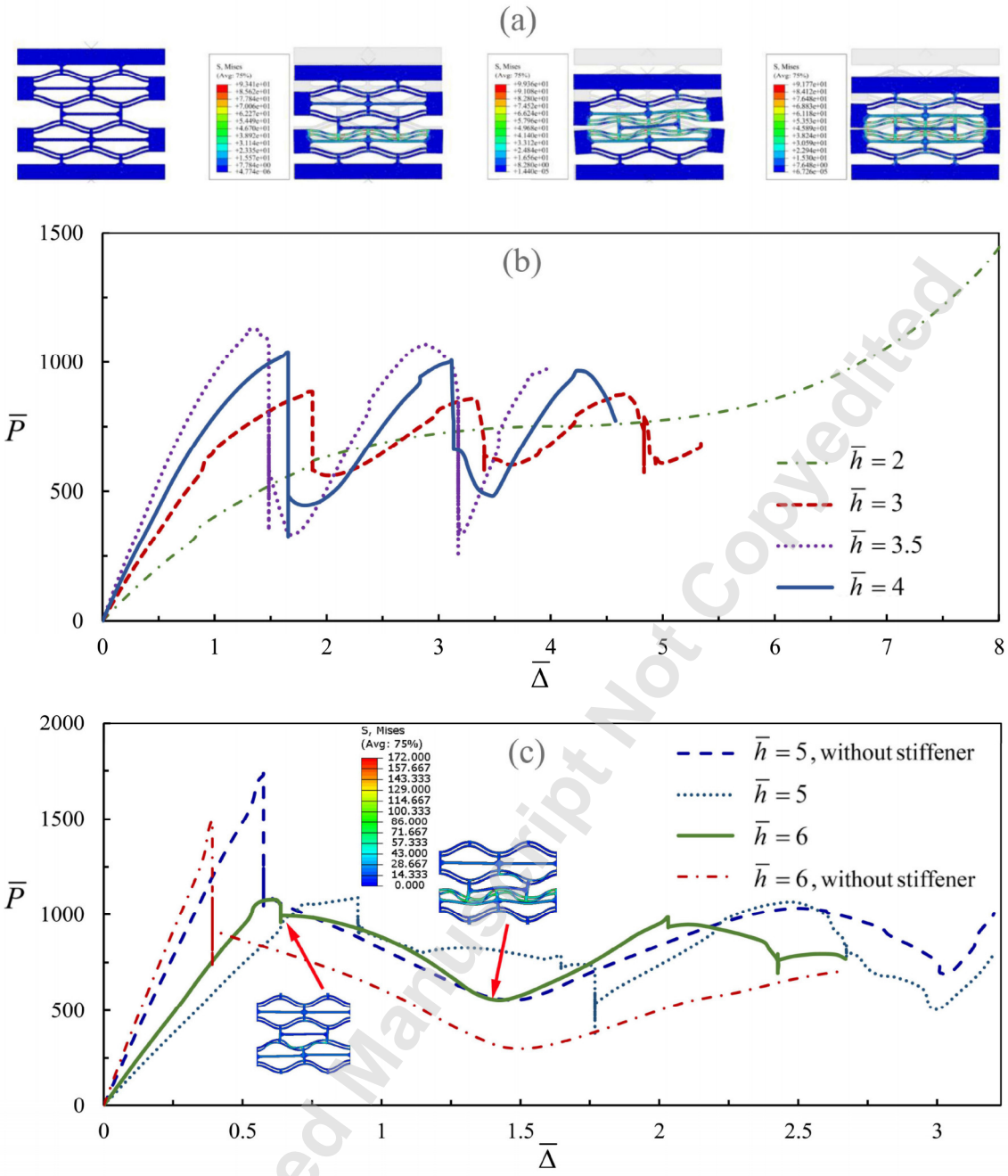

Figure 6 (a) Mises stresses of the NSH unit cell under uniaxial compression load. (b) Force-deformation plot for models with low bistability ratios. (c) Force-deformation plot for models with high bistability ratios (with and without horizontal stiffeners).

A salient feature of the NSH models without the stiffeners and unconstrained boundaries on either side (Figure 6b) is the higher force due to linear lateral deformation followed by a broad peak as the curved beams buckle. The shear stresses accumulated at the joints due to the lack of interconnecting horizontal stiffeners would result in pitch moments and thus instability in the unconstrained structure.

Journal of Applied Mechanics. Received December 21, 2020;
Accepted manuscript posted January 25, 2021. doi:10.1115/1.4049954

Table 2 Comparison of the load and displacement values in the numerical and analytical models

$\bar{h}$	Maximum $\bar{P}$			$\bar{\Delta}$ at Maximum $\bar{P}$		
	Numerical	Analytical	Difference	Numerical	Analytical	Difference
3	885.08	882.3997	0.30%	1.87	1.85	1.19%
3.5	1039.70	964.18	7.26%	1.66	1.49	10.13%
4	1127.36	1124.66	0.24%	1.32	1.48	12.06%
5	1089.17	1168.00	7.24%	0.91	0.86	5.41%
6	1078.04	1159.51	7.56%	0.62	0.54	12.41%

5 Concluding remarks

This work studied the stability of a lattice metamaterial referred to as the negative stiffness honeycomb (NHS) model upon transverse static loading. The honeycomb metamaterial structure was constructed with a pattern of double curved beams fabricated from Polyamide 11, which is a flexible, isotropic material with high ductility.

Given the structure remains entirely nonlinear elastic upon a compressive static load while constraining the mode 2 of deformation, an analytical model was developed based on such simplifying assumptions whereby the relevant differential equation (mathematical model) was derived. The developed mathematical model was utilised to solve the problem and its features were compared with the parametric FE numerical models which were set up and run in the commercial FE code ABAQUS ®14, with a strong agreement between the two models. A salient feature of the model was the pronounced snap-back buckling response as well as the significance of the negative slope in the force-displacement curves at increased bistability ratios. Another feature was the fluctuation in the force-displacement curves, which was more pronounced at higher bistability ratios while the range of $\bar{h} < 3$ rendered a plateau and loss of the desired negative stiffness feature.

The analytical model was thus able to capture the force-deformation path of the system whereby the force is reduced at the expense of the morphed shape of the curved beams. With a slight shift throughout the deformation, the analytical model favourably captured the stiffness degradation, nevertheless the consistency in the quantity $d\bar{P}/d\Delta$ in the two models was maintained throughout the motion.

It was shown that, while in the double curved beams, mode 2 is constrained and the beam would experience bistability with the associated transition from mode 1 to 3, the overall response of the honeycomb structure made of such beams becomes more complex, as relative displacements of the beams may occur which correspond to higher deformation modes. Furthermore, estimating the exact response of the NSH structure is difficult since in practice the buckling phases are interspersed with the global axial deformation of the struts. Snap-through and snap-back may thus occur when the mid-span of the curved beam has travelled downward relative to the interconnecting struts.

Declaration of interests

The authors declare that they have no known competing financial interests or personal relationships that could have appeared to influence the work reported in this paper.

Acknowledgements

This work was supported by the University of Liverpool's Industrial Strategy Pump Priming Fund 2019/20.

6 References

[1] S. Daynes, K. D. Potter, and P. M. Weaver, "Bistable prestressed buckled laminates," *Compos. Sci. Technol.*, vol. 68, no. 15–16, pp. 3431–3437, 2008, doi: 10.1016/j.compscitech.2008.09.036.

[2] H. Y. Jeong, E. Lee, S. Ha, N. Kim, and Y. C. Jun, "Multistable Thermal Actuators Via Multimaterial 4D Printing," *Adv. Mater. Technol.*, vol. 4, no. 3, pp. 1–7, 2019, doi: 10.1002/admt.201800495.

[3] T. Street and K. A. Seffen, "'Morphing' bistable orthotropic elliptical shallow shells," *Proc. R. Soc. A Math. Phys. Eng. Sci.*, vol. 463, no. 2077, pp. 67–83, 2007, doi: 10.1098/rspa.2006.1750.

[4] L. J. Gibson and M. F. Ashby, *Cellular Solids Structure and porperties*, Second. Cambridge: Cambridge University Press, 2001.

[5] T. Tancogne-Dejean, A. B. Spierings, and D. Mohr, "Additively-manufactured metallic micro-lattice materials for high specific energy absorption under static and dynamic loading," *Acta Mater.*, vol. 116, pp. 14–28, 2016, doi: 10.1016/j.actamat.2016.05.054.

[6] L. . Gibson and M. F. Ashby, *Cellular solids*, 2nd ed. Cambridge University Press, 1997.

[7] L. L. Hu, M. Z. Zhou, and H. Deng, "Dynamic crushing response of auxetic honeycombs under large deformation: Theoretical analysis and numerical simulation," *Thin-Walled Struct.*, vol. 131, no. July, pp. 373–384, 2018, doi: 10.1016/j.tws.2018.04.020.

[8] D. Okumura, N. Ohno, and C. Noguchi, "Post-buckling analysis of elastic honeycombs subject to in-plane biaxial compression," *Int. J. Solids Struct. Sci.*, vol. 39, no. 13–14, pp. 3487–3503, 2002, doi: 10.1016/S0020-7683(02)00165-8.

[9] Z. Zheng, J. Yu, and J. Li, "Dynamic crushing of 2D cellular structures: A finite element study," *Int. J. Impact Eng.*, vol. 32, no. 1–4, pp. 650–664, 2005, doi: 10.1016/j.ijimpeng.2005.05.007.

[10] L. Hu, F. You, and T. Yu, "Effect of cell-wall angle on the in-plane crushing behaviour of hexagonal honeycombs," *Mater. Des.*, vol. 46, pp. 511–523, 2013, doi: 10.1016/j.matdes.2012.10.050.

[11] L. L. Hu and T. X. Yu, "Mechanical behavior of hexagonal honeycombs under low-velocity impact - Theory and simulations," *Int. J. Solids Struct.*, vol. 50, no. 20–21, pp. 3152–3165, 2013, doi: 10.1016/j.ijsolstr.2013.05.017.

[12] L. L. Hu and T. X. Yu, "Dynamic crushing strength of hexagonal honeycombs," *Int. J. Impact Eng.*, vol. 37, no. 5, pp. 467–474, 2010, doi: 10.1016/j.ijimpeng.2009.12.001.

[13] B. Hou, H. Zhao, S. Pattofatto, J. G. Liu, and Y. L. Li, "Inertia effects on the progressive crushing of aluminium honeycombs under impact loading," *Int. J. Solids Struct.*, vol. 49, no. 19–20, pp. 2754–2762, 2012, doi: 10.1016/j.ijsolstr.2012.05.005.

[14] B. Hou, S. Pattofatto, Y. L. Li, and H. Zhao, "Impact behavior of honeycombs under combined shear-compression. Part II: Analysis," *Int. J. Solids Struct.*, vol. 48, no. 5, pp. 687–697, 2011, doi: 10.1016/j.ijsolstr.2010.11.005.

[15] Z. Zou, S. R. Reid, P. J. Tan, S. Li, and J. J. Harrigan, "Dynamic crushing of honeycombs and features of shock fronts," *Int. J. Impact Eng.*, vol. 36, no. 1, pp. 165–176, 2009, doi: 10.1016/j.ijimpeng.2007.11.008.

[16] S. Ouyang, Z. Deng, and X. Hou, "Stress concentration in octagonal honeycombs due to defects," *Compos. Struct.*, vol. 204, no. March, pp. 814–821, 2018, doi: 10.1016/j.compstruct.2018.07.087.

[17] S. A. Emam, "A Theoretical and Experimental Study of Nonlinear Dynamics of Buckled Beams, PhD Thesis," 2002.

[18] A. H. Nayfeh and S. A. Emam, "Exact solution and stability of postbuckling configurations of beams," *Nonlinear Dyn.*, vol. 54, no. 4, pp. 395–408, 2008, doi: 10.1007/s11071-008-9338-2.

[19] S. R. Li, Z. C. Teng, and Y. H. Zhou, "Free vibration of heated Euler-Bernoulli beams with thermal postbuckling deformations," *J. Therm. Stress.*, vol. 27, no. 9, pp. 843–856, 2004, doi: 10.1080/01495730490486352.

[20] S. Sun, N. An, G. Wang, M. Li, and J. Zhou, "Snap-back induced hysteresis in an elastic mechanical metamaterial under tension," *Appl. Phys. Lett.*, vol. 115, no. 9, 2019, doi: 10.1063/1.5119275.

[21] C. Ren, D. Yang, and H. Qin, "Mechanical performance of multidirectional Buckling-based Negative Stiffness metamaterials: An analytical and numerical study," *Materials (Basel).*, vol. 11, no. 7, 2018, doi: 10.3390/ma11071078.

[22] A. Rafsanjani, A. Akbarzadeh, and D. Pasini, "Snapping Mechanical Metamaterials under Tension," *Adv. Mater.*, vol. 27, no. 39, pp. 5931–5935, 2015, doi: 10.1002/adma.201502809.

[23] Y. Chen and L. Jin, "Snapping-back buckling of wide hyperelastic columns," *Extrem. Mech. Lett.*, vol. 34, p. 100600, 2020, doi: 10.1016/j.eml.2019.100600.

[24] P. Sareh, P. Chermprayong, M. Emmanuelli, H. Nadeem, and M. Kovac, "Rotorigami: A rotary origami protective system for robotic rotorcraft," *Sci. Robot.*, vol. 3, no. 22, pp. 1–13, 2018, doi: 10.1126/scirobotics.aah5228.

[25] J. G. Mooney and E. N. Johnson, "A Collision-resilient Flying Robot," *J. F. Robot.*, vol. 31, no. 4, pp. 496–509, 2013, doi: 10.1002/rob.21495.

[26] J. Alonso-Mora, T. Naegeli, R. Siegwart, and P. Beardsley, "Collision avoidance for aerial vehicles in multi-agent scenarios," *Auton. Robots*, vol. 39, no. 1, pp. 101–121, 2015, doi: 10.1007/s10514-015-9429-0.

[27] C. Lv, D. Krishnaraju, G. Konjevod, H. Yu, and H. Jiang, "Origami based mechanical metamaterials," *Sci. Rep.*, vol. 4, 2014, doi: 10.1038/srep05979.

[28] P. Sareh, "The least symmetric crystallographic derivative of the developable double corrugation surface: Computational design using underlying conic and cubic curves," *Mater. Des.*, vol. 183, p. 108128, 2019, doi: 10.1016/j.matdes.2019.108128.

[29] K. Liu, T. Tachi, and G. H. Paulino, "Invariant and smooth limit of discrete geometry folded from bistable origami leading to multistable metasurfaces," *Nat. Commun.*, vol. 10, no. 1, pp. 1–10, 2019, doi: 10.1038/s41467-019-11935-x.

[30] P. Cazottes, A. Fernandes, J. Pouget, and M. Hafez, "Bistable buckled beam: Modeling of actuating force and experimental validations," *J. Mech. Des. Trans. ASME*, vol. 131, no. 10, pp. 1010011–10100110, 2009, doi: 10.1115/1.3179003.

[31] B. Camescasse, A. Fernandes, and J. Pouget, "Bistable buckled beam: Elastica modeling and analysis of static actuation," *Int. J. Solids Struct.*, vol. 50, no. 19, pp. 2881–2893, 2013, doi: 10.1016/j.ijsolstr.2013.05.005.

[32] D. M. Correa, T. Klatt, S. Cortes, M. Haberman, D. Kovar, and C. Seepersad, "Negative stiffness honeycombs for recoverable shock isolation," *Rapid Prototyp. J.*, vol. 21, no. 2, pp. 193–200, 2015, doi: 10.1108/RPJ-12-2014-0182.

[33] B. M. Goldsberry and M. R. Haberman, "Negative stiffness honeycombs as tunable elastic metamaterials," *J. Appl. Phys.*, vol. 123, no. 9, 2018, doi: 10.1063/1.5011400.

[34] M. Vangbo, "An analytical analysis of a compressed bistable buckled beam," *Sensors Actuators, A Phys.*, vol. 69, no. 3, pp. 212–216, 1998, doi: 10.1016/S0924-4247(98)00097-1.

[35] J. Qiu, "An Electrothermally-Actuated Bistable MEMS Relay for Power Applications," *Massachusetts Inst. Technol.*, p. 94, 2003.

[36] J. Qiu, J. H. Lang, and A. H. Slocum, "A curved-beam bistable mechanism," *J. Microelectromechanical Syst.*, vol. 13, no. 2, pp. 137–146, 2004, doi: 10.1109/JMEMS.2004.825308.

[37] P. Z. Bazant and L. Cedolin, *Stability Of Structures*, 4th ed. London: World Scientific Publishing Co. Pte. Ltd, 2010.

[38] D. M. Correa, C. C. Seepersad, and M. R. Haberman, "Mechanical design of negative stiffness honeycomb materials," *Integr. Mater. Manuf. Innov.*, vol. 4, no. 1, pp. 165–175, 2015, doi: 10.1186/s40192-015-0038-8.

[39] S. F. Fabrication, A. International, S. Freeform, F. Symposium, A. Additive, and M. Conference, "ADDITIVELY MANUFACTURED CONFORMAL NEGATIVE STIFFNESS HONEYCOMBS D. A. Debeau*, C. C. Seepersad* *Department of Mechanical Engineering, The University of Texas at Austin, Austin, TX 78712," *Solid Free. Fabr. Symp.*, pp. 2170–2187, 2017.